Photoluminescence in ZnO:Co2+ (0.01%−5%) Nanoparticles, Nanowires, Thin Films, and Single Crystals as a Function of Pressure and Temperature: Exploring Electron−Phonon Interactions

ARTICLE *in* CHEMISTRY OF MATERIALS · JANUARY 2014

Impact Factor: 8.35 · DOI: 10.1021/cm403371n

9 AUTHORS, INCLUDING:

Jesus Gonzalez
Universidad de Cantabria
282 PUBLICATIONS **1,995** CITATIONS
SEE PROFILE

Fernando Rodríguez
Universidad de Cantabria
178 PUBLICATIONS **1,340** CITATIONS
SEE PROFILE

Gloria Almonacid
University of Valencia
4 PUBLICATIONS **30** CITATIONS
SEE PROFILE

Alfredo Segura
University of Valencia
217 PUBLICATIONS **3,358** CITATIONS
SEE PROFILE

CHEMISTRY OF MATERIALS

Article

pubs.acs.org/cm

Photoluminescence in ZnO:Co^{2+} (0.01%–5%) Nanoparticles, Nanowires, Thin Films, and Single Crystals as a Function of Pressure and Temperature: Exploring Electron–Phonon Interactions

Carlos Renero-Lecuna,*[,†,‡] Rosa Martín-Rodríguez,[†,‡] Jesus A. González,[¶,‡] Fernando Rodríguez,[¶,‡] Gloria Almonacid,[§,‡] Alfredo Segura,[§,‡] Vicente Muñoz-Sanjosé,[§] Daniel R. Gamelin,[∥] and Rafael Valiente*[,†,‡]

[†]Dpto. Física Aplicada, Universidad de Cantabria, Santander E-39005, Spain

[‡]MALTA-CONSOLIDER Team, [¶]DCITIMAC, Universidad de Cantabria, Santander E-39005, Spain

[§]ICMUV, Departamento de Física Aplicada, Universitat de Valencia, Burjassot (Valencia) E-46100, Spain

[∥]Department of Chemistry, University of Washington, Seattle Washington 98195-1700, United States

Supporting Information

ABSTRACT: This work investigates the electronic structure and photoluminescence properties of Co^{2+}-doped ZnO and their pressure and temperature dependences through high-resolution absorption and emission spectroscopy as a function of Co^{2+} concentration and their structural conformations as a single crystal, thin film, nanowire, and nanoparticle. Absorption and emission spectra of diluted ZnO:Co^{2+} (0.01 mol %) can be related to the $^4T_1(P) \rightarrow {}^4A_2(F)$ transition of CoO_4 (T_d), contrary to $MgAl_2O_4$:Co^{2+} and $ZnAl_2O_4$:Co^{2+} spinels in which the red emission is ascribed to the $^2E(G) \rightarrow {}^4A_2(F)$ transition. We show that the low-temperature emission band consists of a $^4T_1(P)$ zero-phonon line and a phonon-sideband, which is described in terms of the phonon density of states within an intermediate coupling scheme (S = 1.35) involving all ZnO lattice phonons. Increasing pressure to the sample shifts the zero-phonon line to higher energy as expected for the $^4T_1(P)$ state upon compression. The low-temperature emission quenches above 5 GPa as a consequence of the pressure-induced wurtzite to rock-salt structural phase transition, yielding a change of Co^{2+} coordination from 4-fold T_d to 6-fold O_h . We also show that the optical properties of ZnO:Co^{2+} (T_d) are similar, independent of the structural conformation of the host and the cobalt concentration. The Co^{2+} enters into regular Zn^{2+} sites in low concentration systems (less than 5% of Co^{2+}), although some slight shifts and peak broadening appear as the dimensionality of the sample decreases. These structural effects on the optical spectra are also supported by Raman spectroscopy.

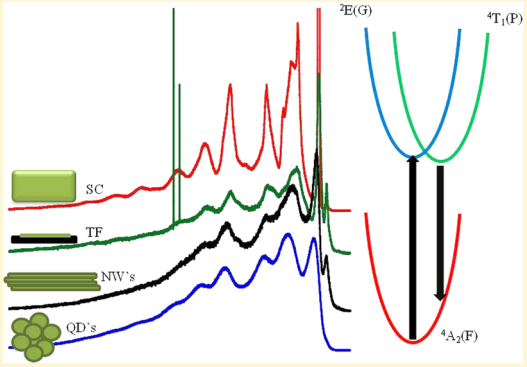

INTRODUCTION

The optical and magnetic properties of the diluted semiconductor ZnO:Co^{2+} have received huge attention because of its current interest in optospintronics.[1] Besides the intrinsic interest of ZnO as bulk material for blue and UV optoelectronics, including light-emitting diodes, lasers, transparent photoconductor (or conductor when doped with Al, Ga), diluted magnetic semiconductors doped with transition-metal ions (Mn, Fe, V, or Co) have had great impact in fundamental and applied research areas. Its application capabilities have increased the possibility to synthesize this material in different structural conformations beyond single crystals as ultrathin films, nanowires, nanoparticles, and quantum wells and dots .

Zinc oxide is a wide-gap IIb–VI semiconductor with a direct gap around 3.4 eV at 300 K. It crystallizes preferentially in the hexagonal wurtzite-type (W) ($P6_3mc$) structure with $a = b =$ 3.249 Å and c = 5.204 Å (γ = 120°),[2] but it also crystallizes in the zinc-blende-type (ZB) ($Pa3$) structure a = 4.868 Å at ambient conditions.[3] A pressure-induced structural phase transition from hexagonal W to cubic rocksalt-type (RS) structure ($Fm3m$) at 10 GPa takes place (a = 4.280 Å).[4]

Following the recent reviews by Özgür[1] and Klingshirn,[5] research on ZnO started in the 1930s[6−8] and knew a considerable development at the end of the 1970s related to optoelectronic applications and also because of the possibility of reducing the structure dimensionality at that time, although most of the research was focused on the optical and electronic properties of bulk samples[9−13] and centered in data collections[14] or in textbooks on semiconductor optics.[15]

Received: October 14, 2013
Revised: December 17, 2013
Published: December 22, 2013

dx.doi.org/10.1021/cm403371n | Chem. Mater. 2014, 26, 1100–1107

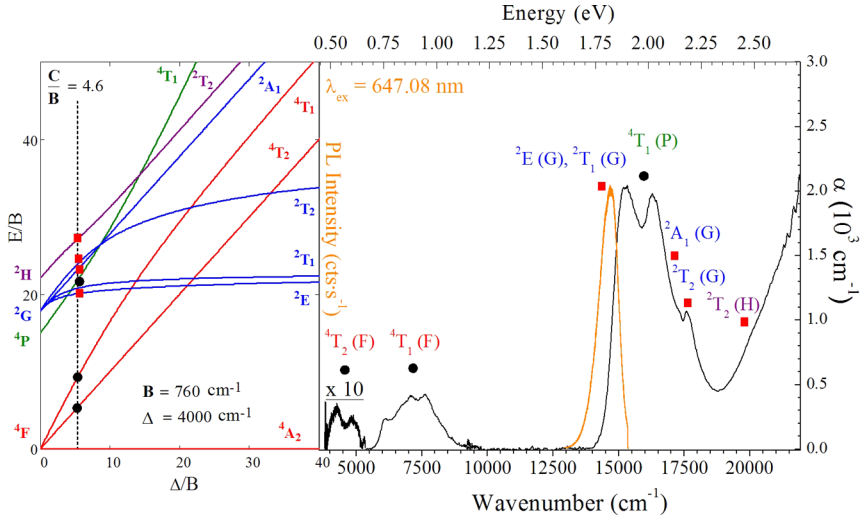

Figure 1. Room temperature absorption and photoluminescence spectra of ZnO:5% Co^{2+} single crystal. Peak assignment corresponds to the electronic crystal-field transitions from the $^4A_2(F)$ ground state of Co^{2+} (T_d) to its excited states. The Tanabe–Sugano diagram of d^7 (T_d) for C/B = 4.6 is included. Black dots represent formally spin-allowed transitions and red squares formally spin-forbidden transitions. The experimental crystal-field energies obtained from the optical spectra are represented by a dotted line at the fit point Δ/B = 5.26. Fitting parameters are B = 0.094 eV (760 cm^{-1}) and Δ = 0.496 eV (4000 cm^{-1}).

The recent renaissance in ZnO research started in the mid-1990s and is mostly related to low-dimensional conformations and the ferromagnetism observed in transition-metal-doped ZnO[16−19] and undoped ZnO nanoparticles,[20] both opening attractive structures for optospintronics applications.[21]

In spite of the huge amount of research activity, there are issues remaining related to the electronic structure of ZnO:Co^{2+} that are deserving of additional attention. Most challenging has been an adequate structural characterization of low-dimensional or nanostructured ZnO:Co^{2+} systems and their interaction with substrates or capping ligands,[20] TM-impurity aggregation (Co^{2+}) in diluted magnetic semiconductors and the important role of extended grain boundary defects.[22,23] In spite of such scrutiny, the correct interpretation of the photoluminescence of Co^{2+} in the ZnO lattice is not well established. Early low-temperature measurements revealed rich fine structure in the optical absorption spectra of very diluted ZnO:Co^{2+} (10 ppm),[24,25] whose peak assignment is still incomplete.

Some interpretations of the origin of the red Co^{2+} photoluminescence at around 700 nm in nanoparticles[26] or epitaxial films[27] of ZnO:Co^{2+} are unclear due to a lack of interpretation in the ZnO:Co^{2+} single crystals. This assignment was the base of the photoluminescence interpretation given by Schulz and Thiede years later.[28] Therefore, the low-temperature fine structure and the high-temperature broadband features observed in the absorption and photoluminescence spectra deserve clarification. Here, we investigate the origin of the rich fine structure observed in the low temperature electronic spectra of ZnO:Co^{2+} single crystals. We interpret the data mainly in terms of electron–phonon coupling between the localized crystal-field Co^{2+} d-orbital states and ZnO phonons. The optical spectra of ZnO:Co^{2+} single crystal will be compared with the corresponding spectra of thin-films, nanowires, and nanoparticles, as well as the effect of increasing Co^{2+} concentrations, to investigate the influence of quantum confinement and size effect with their corresponding dimensionality. Furthermore, we explore possible Co–Co short- and long-range interaction by the presence of extra peaks in the low temperature luminescence spectra.[29]

For these purposes, the application of an external pressure is crucial to unveil the origin of photoluminescence and Co^{2+} excited states through pressure shifts.

EXPERIMENTAL METHOD

ZnO:Co^{2+} (5%) (high Co^{2+} concentration) as a single crystal was grown as described in ref 30 using the hydrothermal method. Low Co^{2+} concentration ZnO:Co^{2+} (0.01%) was prepared by the vapor-phase transport method described elsewhere.[31,32] As source material, high-purity ZnO powders and Co_3O_4 (99.99%) were mixed in ethanol in a stoichiometric proportion and dried in an oven at 60 °C for 24 h. Once the sample was dried, the powders were pressed up to 10 MPa. Then, the pellet was heated up to 950 °C to achieve a good diffusion of Co^{2+} ions in the host lattice for around 10 h. The pellet was crushed in an agatha mortar, and the final powder was placed in a graphitized evacuated quartz ampule in an horizontal tubular oven with a well-stabilized thermal gradient. The oven was heated with a set point of 950°–750° on both sides of the gradient.

ZnO:Co^{2+} thin-films were synthesized by pulsed laser deposition using as a target the above-mentioned pellets on a c-axis-oriented sapphire substrate, as described in Martinez-Criado et al.[33] The thickness was determined by optical absorption through the interference pattern produced by the nanolayer. Nanowires and nanoparticles were obtained following the methods described elsewhere.[34,35]

Unpolarized confocal micro-Raman and luminescence spectroscopy were performed in all samples by means of a triple monochromator (Jobin-Yvon, Model T64000) in subtractive-mode backscattering configuration equipped with a liquid-N_2-cooled CCD detector. The 514.32 and 647.08 nm lines of an Ar^+–Kr^+ laser were focused on the sample with a 20× objective for micro-Raman and luminescence spectroscopy, and the laser power was kept below 4 mW in order to avoid laser-heating effects. The laser spot was 2 μm in diameter, and the spectral resolution was better than 0.6 cm^{-1} in all cases. Raman spectra were fitted to Lorentzian profiles to get the full width at half-maximum (fwhm), intensity, and peak position. The Raman technique was used to check the sample structure through the characteristic first-order modes (E_2^{low} and E_2^{high}) as well as to check for Co-related precipitates like metallic cobalt, CoO, and so forth, which have been reported in highly Co-concentrated samples.[30]

dx.doi.org/10.1021/cm403371n | Chem. Mater. 2014, 26, 1100–1107

Absorption spectra, at ambient conditions and low temperature, were obtained on a Cary 6000i (Varian) in the 200−1800 nm (UV−vis) region, and a Perkin-Elmer Lambda 9 absorption spectrophotometer was used to take the 1000−3200 nm (NIR) spectra. A microstatHe Oxford Instruments open He-cycle microcryostat was used for the low temperature luminescence experiments. Hydrostatic pressure experiments in the 0−10 GPa range at room temperature were carried out on a membrane-type diamond anvil cell (DAC). For high-pressure low-temperature studies, a cryo-DAC-Mega from easyLab was attached to a closed-circuit cryostat DISPLEX DE-202 (0−6 GPa pressure range). In all cases, 200 μm thickness Inconel gaskets were preindented and suitable 200 μm diameter holes were perforated with a Betsa motorized electrical discharge machine. The DAC was loaded with a suitable single crystal and ruby microspheres (<10 μm diameter) with paraffin oil as the pressure-transmitting medium. The pressure and temperature were calibrated from the ruby photoluminescence through the R_1 and R_2 peak shifts and their relative intensity, respectively.[36,37]

RESULTS AND DISCUSSION

Background: Optical Single-Crystal Absorption and Photoluminescence Spectra of ZnO:Co^{2+}. Figure 1 shows the room temperature absorption and visible photoluminescence spectra corresponding to single crystals of Co^{2+}-doped ZnO (5 mol %). The absorption spectrum is identical to those reported in the early 1970's for very dilute samples (10 ppm Co^{2+}).[24,25,38] Both the zero-phonon line (ZPL) (estimated from low temperature absorption and emission spectra), and the rich band structure are identical and independent of the cobalt concentration between 10 and 5×10^4 ppm.

The peak assignment and calculated positions for the absorption bands were made on the basis of the Tanabe−Sugano procedure[39,40] and collected in Table 1. It must be noted that the calculated positions correspond to the centroid maximum, which coincides with the peak position itself, in the case of narrow peaks, if the phonon-sideband intensity is negligible with respect to the electronic origin (i.e., ZPL). If the phonon-sideband is dominant, as for strong electron−phonon coupled transitions ($S \gg 1$), then the calculated position corresponds to the band centroid. A rule of thumb for distinguishing between narrow and broad absorption bands is provided by the Tanabe−Sugano diagram, d^3 (O_h) or d^7 (T_d) in the present case, because their $E(\Delta,B)$ curves have a small slope (zero) or big slope $\partial(E/B)/\partial(\Delta/B)$, respectively. Sometimes, there are excited-state-crossover points in the TS diagram, giving rise to state mixing, mediated by the spin−orbit interaction, and their manifestation in the absorption spectra can be a mix of narrow-broad band character as well. The $^2E(G) \rightarrow {}^4A_2(F)$ and $^4T_1(P) \rightarrow {}^4A_2(F)$ transitions observed at 1.93 eV (15 575 cm^{-1}) and 2.10 eV (16 900 cm^{-1}), respectively, in the PL and absorption spectra as a function of temperature in $MgAl_2O_4:Co^{2+}$ are examples of this behavior.[40] Ferguson et al. obtained similar results in $ZnAl_2O_4:Co^{2+}$.[41] This comparison is interesting because both compounds share the same Co^{2+} T_d coordination, but in the spinels, no further distortion is present. Peak assignment for these systems is made on the basis of Tanabe−Sugano calculations taking into account the crystal-field strengths (Δ) at the tetrahedral Co^{2+} sites of these two spinels. The assignment is not trivial because the reduced crystal-field strength, Δ/B, is located around the $^2E(G)$, $^4T_1(P)$ excited-state crossover. The low-temperature red emission, thus, originates either from $^2E(G)$ or $^4T_1(P)$, depending on whether the $^2E(G)$ configurational curve minimum is lower than that of the $^4T_1(P)$ state. One simple way to identify which one is the emitting state at low temperature is through lifetime measurements. In fact the main $^2E(G) \rightarrow {}^4A_2(F)$ spin-flip transition has an associated transition probability at least an order of magnitude smaller than the main $^4T_1(P) \rightarrow {}^4A_2(F)$ transition, and consequently, longer emission lifetimes are expected for the former transition. For the ZnO:Co^{2+} low temperature PL spectra a luminescence lifetime, τ = 15 ns, has been measured (see Supporting Information Figure 1S), 2 orders of magnitude smaller than the one expected for the $^2E(G) \rightarrow {}^4A_2(F)$ transition. For comparison, the luminescence lifetime in $MgAl_2O_4:Co^{2+}$, τ = 3 μs at 6 K, decreases with temperature down to τ = 0.3 μs at 200 K, thus indicating that the long-lived $^2E(G)$ state is the only one populated at low temperature.[40] Thermal population of the short-lived $^4T_1(P)$ increases the transition probability, yielding a PL lifetime decrease. The short PL decay time of ZnO:Co^{2+} suggests substantial $^4T_1(P)$ character in the emitting state.[40]

The spectra of ZnO:Co^{2+} in Figure 1 are very similar to $MgAl_2O_4:Co^{2+}$, as expected, because Co^{2+} has a CoO_4 (T_d) coordination structure in both cases. However, some significant differences must be considered in the ZnO:Co^{2+} assignment. (1) The $MgAl_2O_4:Co^{2+}$ crystallizes in the spinel structure (cubic $Fd\bar{3}m$, a = 8.085(4) Å[42]), where Co^{2+} impurities substitute Mg^{2+} at the T_d site (R_{Mg-O} = 1.918 Å), whereas ZnO:Co^{2+} crystallizes in the wurtzite-type (W) structure described above (R_{Zn-O} = 1.98 Å). (2) The band gap of both lattices are quite different: 10 eV in $MgAl_2O_4:Co^{2+}$ [43,44] and 3.4 eV in W−ZnO.[1] These differences can affect Δ and the B and C Racah parameters by the different cation−oxygen distance and crystal structure provided by the two crystal hosts and can also affect the transition probabilities because of the much shallower photoionization states in ZnO.[45−47]

Table 1 compares the absorption peak energies in $MgAl_2O_4:Co^{2+}$ and ZnO:Co^{2+}, including some structural

Table 1. Peak Assignment and Experimental Transition Energies Taken from the Optical Absorption Spectra of ZnO:Co^{2+} at Room Temperature in Figure 1 and Calculated Energies for Co^{2+} in T_d Symmetry[a]

	$MgAl_2O_4:Co^{2+}$		ZnO:Co^{2+}	
absorption peak assignment for $Co^{2+}(T_d)$	$E_{experimental}$ (eV)	$E_{calculated}$ (eV)	$E_{experimental}$ (eV)	$E_{calculated}$ (eV)
$^4A_2(F) \rightarrow {}^4T_2(F)$		0.52	0.54	0.50
$\rightarrow {}^4T_1(F)$	0.90	0.89	0.88	0.86
$\rightarrow {}^2E(G)$	1.93	1.93	1.89	1.89
$\rightarrow {}^2T_1(G)$	2.00	2.00		1.96
$\rightarrow {}^4T_1(P)$	2.10	2.13	2.02	2.04
$\rightarrow {}^2A_1(G)$	2.25	2.23	2.19	2.17
$\rightarrow {}^2T_2(G)$	2.34 (sh)	2.33		2.25
$\rightarrow {}^2T_2(H)$	2.60	2.60		2.55
B	0.098		0.094	
C	0.044		0.434	
C/B	4.500		4.605	
Δ	0.520		0.496	
Δ/B	5.30		5.26	
σ	0.014		0.044	

[a]The calculated energies were obtained by fitting the experimental energies to the energy terms of a d^3 electron configuration.[39] The fit B and C Racah parameters and crystal-field splitting, Δ_{CF}, are collected together with the standard deviation, σ. Data corresponding to $MgAl_2O_4:Co^{2+}$ [40] are also included for comparison purposes.

dx.doi.org/10.1021/cm403371n | Chem. Mater. 2014, 26, 1100−1107

relevant parameters. The crystal-field strength in ZnO:Co^{2+} (Δ = 0.496 eV) is slightly reduced compared to $MgAl_2O_4$:Co^{2+} (Δ = 0.52 eV), whereas B is more similar (B = 0.094 and 0.098 eV, respectively). The relative decrease of both Δ and B is actually the same: 0.496/0.52 = 0.953 and 0.094/0.098 = 0.959. Δ reduction must be ascribed to the longer R_{Zn-O} as compared to R_{Mg-O}, whereas B reduction should be associated with the higher Co−O bond covalency in ZnO compared to the highly ionic $MgAl_2O_4$:Co^{2+}. Together, these effects reduce Δ/B from 5.30 in $MgAl_2O_4$:Co^{2+} to 5.26 in ZnO:Co^{2+}, approaching the $^4T_1(P)$ to $^2E(G)$ excited-state crossover. Importantly, although the centroid of the $^4T_1(P)$ band is above the $^2E(G)$ peak (Table 1), its ZPL is below $^2E(G)$ in ZnO:Co^{2+} (see next section). This situation could be anticipated taking into account the redshift of $^4T_1(P)$ on passing from $MgAl_2O_4$:Co^{2+} ($E(^4T_1(P))$ = 2.10 eV) to ZnO:Co^{2+} ($E(^4T_1(P))$ = 2.02 eV) (Table 1) and the fact that the ZPL energy difference between $^4T_1(P)$ and $^2E(G)$ is only 0.019 eV in $MgAl_2O_4$:Co^{2+}.[40] According to this energy balance, the possibility of $^4T_1(P)$ as emitting state in ZnO:Co^{2+} is likely. This idea reinforces the conclusion drawn from the short luminescence lifetime measured at low temperature (τ < 15 ns, shown in Supporting Information Figure 1S).

ORIGIN OF THE NARROW-PEAK STRUCTURE IN ZNO:CO^{2+}: ELECTRON−PHONON COUPLING AND EXCHANGE EFFECTS

Previous studies[6,10,25,40,48−50] on $MgAl_2O_4$:Co^{2+} and $ZnAl_2O_4$:Co^{2+} have concluded that $^2E(G)$ is the Co^{2+} emitting state at low-temperature. The situation for ZnO:Co^{2+} is less clear. Polarized absorption studies have permitted identification of the zero-phonon lines (ZPLs) at 1.8828 and 1.8850 eV (15 186 cm^{-1} and 15 204 cm^{-1}, respectively), attributable to the $^4A_2(F) \rightarrow {}^2E(G)$ spin-flip transition, split by the trigonal crystal field (C_{3v}) and the spin−orbit interaction by 2.2 meV (18 cm^{-1}).[25] Figure 2 shows the emission and absorption spectra of ZnO:Co^{2+} at low temperature. The $^2E(G)$ peaks around 1.8828 and 1.8850 eV can be clearly observed. However, there are two additional unassigned narrow lines at 1.8781 and 1.8775 eV (15 148 cm^{-1} and 15 143 cm^{-1}). Their separation of 0.6 meV (5 cm^{-1}) is associated with the zero-field splitting of the $^4A_2(F)$ ground state, and their relative intensity changes with temperature in absorption but does not vary in emission. In fact, these two lines are the main feature of the emission spectrum at low temperature (Figure 2). These two ZPL components have about the same intensity in emission, but in absorption, the higher energy component (1.8850 eV) is three times more intense than the lower energy component (1.8828 eV), reflecting the different population of the two ground-state spinors at 8 K. The emission spectrum consists of a complex sideband structure that is constructed from these two lines, but no evidence of emission from $^2E(G)$ is detected. Whether these lines are associated with $^4T_1(P) \rightarrow {}^4A_2(F)$ ZPL and whether the fine features appearing at lower energy are associated with vibrational couplings or exchange effects will be discussed below.

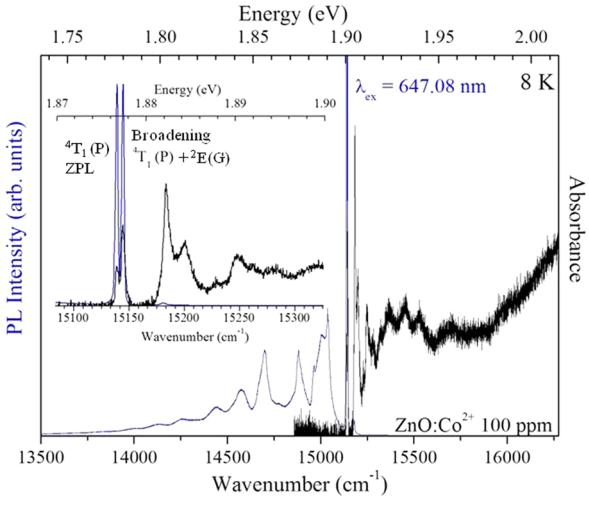

Figure 2. Emission (blue) and absorption (black) of ZnO:Co^{2+} (0.01%) single crystal in the visible region at 8 K. The inset shows an expanded view of the $^4T_1(P)$ zero-phonon line. The excitation wavelength was 647.08 nm.

Figure 3 compares the 8 K emission spectrum with the phonon density of states (PDOS) calculated for ZnO using the phonon frequencies obtained from Raman spectroscopy and inelastic neutron scattering.[51] This comparison provides strong evidence that the emission spectrum consists of a phonon sideband constructed from the ZPLs at 1.8781 and 1.8775 eV (15 148 cm^{-1} and 15 143 cm^{-1}). The fair agreement between the phonon sideband and PDOS indicates that the electron−

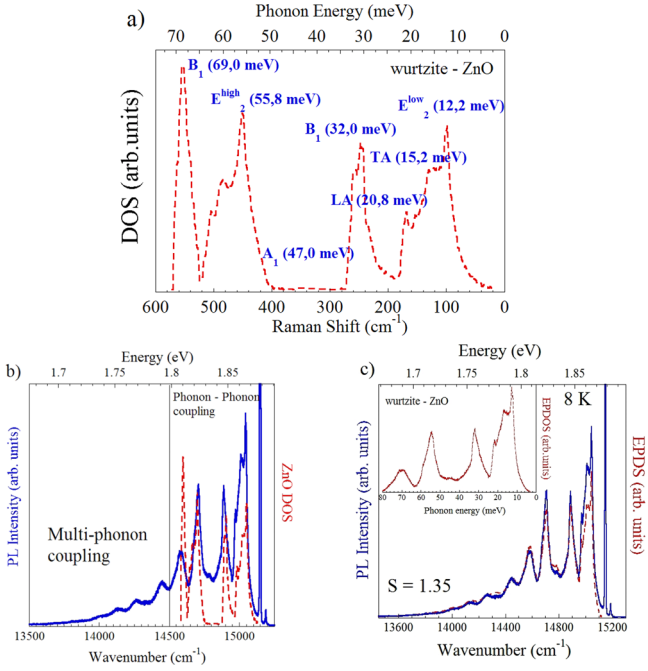

Figure 3. (a) Calculated PDOS of ZnO in the wurtzite structure with the assignment of the vibrational modes from ref 51. (b) Emission spectra (blue) of ZnO:Co^{2+} (0.01%) single crystal around the ZPL at 8 K. The sideband is compared with the ZnO PDOS[51] (red dotted line). Note the good agreement between the sideband maxima and the PDOS maxima, as well as their shape, when PDOS is built upon the ZPL line at 15 148 cm^{-1}. (c) Simulation of the phonon-sideband of the 8 K emission spectrum using the EPDOS depicted in the inset derived from the emission spectra. The simulation was done by convoluting the one-phonon density of sates (red dotted line) to the fifth order coupling, B_5, with B_n being the n-phonon order convoluted DOS, following the procedure given in ref 52, using a Huang−Rhys parameter of S = 1.35 and the equation for the effective one-phonon DOS, EPDOS = $e^{-S}\sum_{n=1}^{N}((S^nB_n)/n!)$.

dx.doi.org/10.1021/cm403371n | Chem. Mater. 2014, 26, 1100−1107

phonon coupling involves all phonons with almost the same strength, and no significant variation of phonon energies is detected when phonons couple to this electronic state of Co^{2+}. The similarity between Co and Zn masses does not alter the phonon frequencies as determined from direct measurements or through the phonon-sideband of the Co^{2+} emission. On the basis of the emission spectrum, we have deduced an effective one-phonon density of state (DOS) (inset of Figure 3c). The phonon sideband can be accounted for on the basis of the effective one-phonon DOS using a Huang−Rhys parameter of $S = 1.35$. This value corresponds to an intermediate electron−phonon coupling regime but is higher than that expected for weak coupling with the spin-flip $^2E(G) \rightarrow {}^4A_2(F)$, and we therefore associate the ZPLs at 1.8781 and 1.8775 eV (15 148 cm^{-1} and 15 143 cm^{-1}) to the first spinor of the $^4T_1(P)$ state. ZPLs of the other $^4T_1(P)$ spinors occur at higher energy, overlapping the $^2E(G)$ peak and making their identification in the low-temperature emission spectrum difficult.

The evolution of the emission and absorption spectra with temperature around the electronic origins is shown in Figure 4.

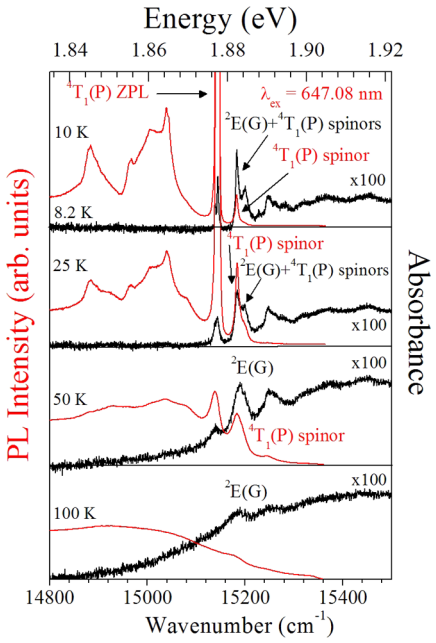

Figure 4. Temperature dependence of the optical absorption and luminescence spectra from the ZnO:Co^{2+} (0.01%) single crystal in the 8−100 K range at ambient pressure. Note that the ZPLs associated with a $^4A_2(F) \rightarrow {}^2E(G)$, $^4T_1(P)$ absorption transitions broadens and persists for $^2E(G)$ but disappears for $^4T_1(P)$. In emission, only the ZPL $^4T_1(P)$ associated with $^4T_1(P) \rightarrow {}^4A_2(F)$ is observed at low temperature (15 143 cm^{-1}). A hot ZPL at 15 186 cm^{-1} associated with the $^4T_1(P)$ spinor of higher energy rises with temperature at the expense of the first ZPL. Its position coincides with the $^4A_2(F) \rightarrow {}^2E(G)$ transition energy, and its emission is narrower than in absorption because of the joint presence of $^2E(G)$ and $^4T_1(P)$ ZPLs.

A hot ZPL located at 1.8828 eV (15 186 cm^{-1}) appears at the expense of the first ZPL at 1.8781 eV (15 148 cm^{-1}) as temperature increases. Above 20 K another ZPL at 15 168 cm^{-1} is observed, indicating that all these ZPLs are $^4T_1(P)$ spinors. The position of this emission hot line coincides with the $^2E(G)$ peak position observed in absorption. However, the hot emission ZPLs actually correspond to $^4T_1(P)$ instead of $^2E(G)$ given that the transition probability $^2E(G) \rightarrow {}^4A_2(F)$ is much smaller than the $^4T_1(P) \rightarrow {}^4A_2(F)$ probability because of the spin selection rule. Even if we populate both the $^2E(G)$ state and other $^4T_1(P)$ spinors with increasing temperature, the emitted photons are mostly from $^4T_1(P)$; hence, these are the only ZPLs observed in emission. Although the ZPL of $^2E(G)$ and one of the $^4T_1(P)$ spinors are energy resonant, they are spatially displaced along the nuclear distortion coordinate in a configurational coordinate diagram; therefore, the interaction among them is rather weak.

A detailed observation of the 25 K emission spectrum in Figure 4 reveals the presence of a shoulder at 1.867 eV (15 080 cm^{-1}). This indicates that the same phonon sideband associated with the first ZPL is also constructed from the hot ZPL. This interpretation also explains why ZPLs in absorption appear as narrow features for the first $^4T_1(P)$ spinor but more intense and broadened for the other spinors at 1.8828 and 1.8850 eV (15 186 cm^{-1} and 15 204 cm^{-1}). In fact, both $^4T_1(P)$ and $^2E(G)$ contribute to these higher-energy ZPLs and, thus, appear as broad features in absorption. The main phonon features in the absorption spectrum are constructed from the first $^4T_1(P)$ spinor at 1.8781 eV (15 148 cm^{-1}) and not from the intense ZPL at 1.8828 eV (15 186 cm^{-1}). The latter is mainly $^2E(G)$, and most of the intensity is concentrated in the ZPL; its associated phonon sideband is negligible in comparison to $^4T_1(P)$. This behavior is confirmed by the temperature evolution of the absorption spectrum. As temperature increases, the ZPLs broaden, the $^4T_1(P)$ ZPLs disappearing toward a broad phonon-sideband, but $^2E(G)$ remains as a visible bump in the absorption band, thus confirming $^2E(G)$ has a negligible phonon-sideband intensity.

The present ZPL assignment is also supported by high-pressure experiments at low temperature (Figure 5). The two emission ZPLs experience the same pressure blue-shift as $\partial E/\partial P$ = +1.41 meV/GPa (+11.4 cm^{-1} /GPa). A slightly smaller pressure coefficient (0.9 meV/GPa) for this electronic transition was obtained through absorption measurements in high Co content thin film samples.[53] If one of the two ZPLs

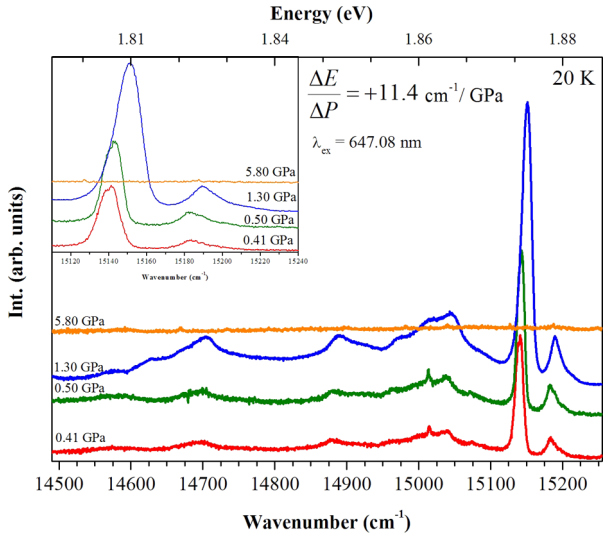

Figure 5. Pressure dependence of the emission spectra of ZnO:Co^{2+} (0.01%) single crystal at 20 K. The inset shows the shift of the $^4T_1(P) \rightarrow {}^4A_2(F)$ ZPL with pressure. The pressure-induced blueshift of the two ZPLs is consistent with the peak assignment to $^4T_1(P)$ spinors. The $^2E(G) \rightarrow {}^4A_2(F)$ peaks should shift to lower energy according to expectations from the TS diagram.

dx.doi.org/10.1021/cm403371n | Chem. Mater. 2014, 26, 1100−1107

would be associated with a different state, the pressure shift should be somewhat different, with $^2E(G)$ probably shifting to lower energies, as ruby does. Therefore, the pressure shift supports the assignment of the ZPL origin as $^4T_1(P)$. The decrease of emission intensity with pressure and its disappearance at 5.8 GPa is noteworthy. A similar result was also found in $MgAl_2O_4:Co^{2+}$ and was attributed to pressure-induced nonradiative multiphonon relaxation to the $^4T_1(F)$ excited state.[40] This conclusion is the opposite of what is generally accepted for luminescent impurity systems, where larger photoluminescence intensity is expected for transition metal ions placed in smaller sites. Four-coordinated Co^{2+} systems, like those attained in $MgAl_2O_4:Co^{2+}$ and $ZnO:Co^{2+}$, behave oppositely; thus, PL is favored upon volume expansion. Raman measurements show that the luminescence quenching in $ZnO:Co^{2+}$ is due to a pressure induced W to RS phase transition. This will be published in a forthcoming work. Also, no trace of exchange coupling mechanism between Co^{2+} ions through superexchange interaction or through conduction band (indirect exchange) is observed in emission or absorption spectra. Therefore, none of the fine structure observed in the emission spectra are due to exchange-coupling mechanisms.

EFFECTS OF COBALT CONCENTRATION AND STRUCTURAL CONFORMATION AS THIN FILMS, NANOWIRES, AND NANOPARTICLES

Concentration Dependence. Figure 6 shows the emission spectra of $ZnO:Co^{2+}$ for cobalt concentrations x = 0.0001 and 0.05. The absorption spectra are similar in both systems with the exception of the peak broadening produced as Co^{2+} concentration increases. The main effect on Co^{2+} concentration can be observed in the $^4T_1(P)$ ZPL doublet. Within experimental accuracy (0.6 cm^{-1}), their position does not change with Co^{2+} concentration ranging from x = 0.0001 to 0.05, suggesting that the average crystal-field splitting is not dependent on concentration and, therefore, no significant variation of lattice volume is expected with Co^{2+} doping in this concentration range. In fact, EXAFS measurements of Co−O distance in thin films do not detect any significant change even at Co^{2+} proportions as high as 26%.[33] The observation of the same frequencies for the ZnO Raman active modes, irrespective of the Co^{2+} concentration, supports this conclusion. However, the line width at half-maximum of the two Lorentzian-shaped ZPLs broadens from 2.4 cm^{-1} to 5 cm^{-1} on passing from x = 0.0001 to 0.05. We associate this broadening to the Co^{2+} site distribution in the $Zn_{1-x}Co_xO$ host. Statistically, the main Co^{2+} site for the diluted sample (x = 0.0001) mostly corresponds to the cluster CoO_4 tetrahedron surrounded by 12 corner-sharing ZnO_4 tetrahedra (99.9%), named $CoO_4-(ZnO_3)_{12}$. However, the probability of these clusters is reduced to 54% for x = 0.05, and other clusters involving Co−O−Co links appear: $CoO_4-(ZnO_3)_{11}(CoO_3)_1$ (34%), $CoO_4-(ZnO_3)_{10}(CoO_3)_2$ (10%), and so on. The presence of Zn^{2+} and Co^{2+} in the next neighbor shell produces a slight ZPL shift that depends on the relative number of Zn^{2+}/Co^{2+} ions in the cluster. Taking into account that the 4-fold-coordinated ionic radii are 0.60 and 0.67 Å, respectively,[54] the Co^{2+}-rich cluster will experience a bigger volume and, thus, an axial stress component of the crystal field compared to the isolated CoO_4 unit. This distortion will cause a ZPL distribution around the central position of the cluster as the Co^{2+} concentration increases, in agreement with observations (Figure 6). These effects are not observed in Raman spectra because phonons indeed are long-range properties and broadening due to small Co^{2+} to Zn^{2+} mass difference (59 and 63, respectively).

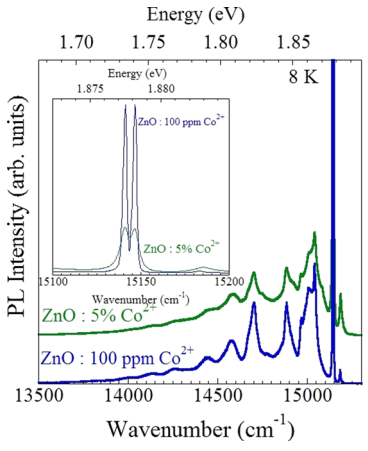

Figure 6. Effect of Co^{2+} concentration on 8 K emission spectrum of $ZnO:Co^{2+}$ single crystal around the ZPLs. The inset shows the peak broadening of the ZPLs from 2.5 cm^{-1} to 5.4 cm^{-1} on passing from $[Co^{2+}]$ = 0.01 mol % to 5 mol %. No additional peak due to $Co^{2+}-Co^{2+}$ exchange interaction or peak position shifts depending on $[Co^{2+}]$ are observed in the luminescence spectra in the studied concentration range. This result correlates with Raman spectroscopy data indicating that within 0.6 cm^{-1}; ZnO phonon frequencies at Γ do not change with cobalt concentration over this range either.

Influence of the Structural Conformation: Single-Crystal, Thin-Film, Nanowire, and Nanoparticles. Figure 7 shows the low-temperature emission spectra of $ZnO:Co^{2+}$ for different dimensionalities of the host: single-crystal (SC), thin-film (TF), nanowire (NW), and nanoparciles (NP). The low-temperature emission spectra indicate that (1) Co^{2+} enters at the Zn^{2+} tetrahedral sites irrespective of the ZnO dimensionality, (2) no evidence of nearby oxygen vacancy effects is observed because peak positions and phonon sideband shapes are similar for all conformations, but any axial stress field would yield in a significant photoluminescence redshift,[55] and (3) there is a peak broadening affecting both the ZPL and the

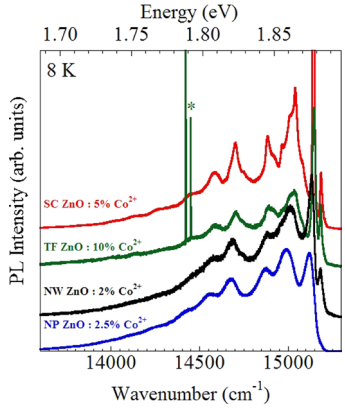

Figure 7. Effect of structural conformation on the emission spectrum of $ZnO:Co^{2+}$. The spectra correspond to single crystal (SC), thin film (TF), nanowire (NW), and nanoparticle (NP) with $[Co^{2+}]$ = 5, 10, 2, and 2.5 mol %, respectively. Note the peak broadening and overall red shift with decreasing crystal dimensionality. The R_1 and R_2 Cr^{3+} lines of the sapphire substrate in the TF sample are marked with *. Excitation wavelength used in all the experiments is 647.08 nm.

dx.doi.org/10.1021/cm403371n | Chem. Mater. 2014, 26, 1100−1107

associated phonon sideband, which increases with the Co^{2+} concentration as well as dimensionality reduction. This latter effect is due to crystal field inhomogeneities of Co^{2+} sites in nanostructures.[56] Dimensionality reduction increases the phonon wave-vector uncertainty, giving rise to broadening in both the ZPLs and the phonon sideband with decreasing system dimensionality. Furthermore, there is an overall redshift of the $^4T_1(P)$ emission when passing from TF to NW and NP. According to the pressure-induced blue-shift observed in SC, these results show how NP formation implies a decrease of the effective pressure acting on Co^{2+} with increasing surface area (i.e., NP seems to be less dense than SC following the Co^{2+} emission spectrum as pressure probe). ZnO densification occurs on passing from NP to NW and TF. The largest Co^{2+}-emission blue-shift is observed in TF, even more than in SC. We ascribe this singular behavior to a strain field imposed by the sapphire substrate. The relevant in-plane lattice parameter in C-face oriented sapphire is the *a* parameter of the hexagonal oxygen sublattice (0.2751 nm). The ZnO lattice parameter is 18% larger, which leads to a strong compressive strain for films below 200 nm thick. For the films studied here, around 100 nm thick, the compressive strain can be close to 0.1%.[57] It is also remarkable that room temperature red photoluminescence is also observed (see Supporting Information Figure 3S) in all the samples with different dimensionalities (from single crystal to nanoparticles).

■ CONCLUSIONS

We have demonstrated that Co^{2+} photoluminescence in ZnO:Co^{2+} originates from the short-lived (τ < 15 ns) $^4T_1(P)$ state at low temperature. The photoluminescence spectra show a structured sideband built upon the $^4T_1(P)$ ZPLs as a result of electron−phonon coupling to all ZnO phonons. The phonon sideband shape agrees well with the PDOS of ZnO. We show that the crystal-field at the Co^{2+} site is close to the excited-state crossover [$^4T_1(P) \leftrightarrow {}^2E(G)$]. In contrast with $MgAl_2O_4$:Co^{2+}, the minimum of the configurational energy diagram in ZnO:Co^{2+} is not $^2E(G)$ but corresponds to $^4T_1(P)$, making this the emitting state. There is no evidence of exchange-induced electronic transitions either in emission or absorption, suggesting that Co^{2+} is isolated for x = 0.0001. We have established that, instead of enhancing the excited-state crossover phenomena, pressure (or volume compression) reduces Co^{2+} photoluminescence at tetrahedral sites and eventually suppresses it (photoluminescence quenching) at the wurtzite to rock salt structural phase transition pressure. This conclusion has important effects on the photoluminescence efficiency of ZnO:Co^{2+} in different structural conformations, provided that they lead to lattice expansion. The Co^{2+} photoluminescence enhancement found in ZnO:Co^{2+} NP in comparison to TF or NW are ascribed to local expansion effects around Co^{2+} in a nanoparticle, attributable to surface relaxation effects.

■ ASSOCIATED CONTENT

Ⓢ Supporting Information

Photoluminescence lifetime, TEM of nanoparticles. This material is available free of charge via the Internet at http://pubs.acs.org.

■ AUTHOR INFORMATION

Corresponding Authors

*C. Renero-Lecuna. E-mail:carlos.renero@unican.es.

*R. Valiente. E-mail:rafael.valiente@unican.es.

Notes

The authors declare no competing financial interest.

■ ACKNOWLEDGMENTS

The authors thank the Spanish Ministerio de Ciencia e Innovación for the FPI grant (ref no. BES-2009-013434) and the projects (ref nos. MAT2011-28868-C02-1 and MAT2012-38664-C02-1.), and MALTA-CONSOLIDER INGENIO 2010 project (ref no. CSD2007-00045). Also C.R.-L. thanks specially Vicente Marín-Borrás, from the Univeristy of Valencia (Department of Applied Physics,) for his help growing the ZnO:Co^{2+} (0.01% ppm) single crystal, Belén Ortiz and Carmen Pesquera, from the University of Cantabria, Department QuIPRe (Qca. e Ing. de Procesos y Recursos), for the help in the nanowires synthesis, and Lidia Rodríguez-Fernández for the TEM images.

■ REFERENCES

(1) Özgür, Ü.; Alivov, Y. I.; Liu, C.; Teke, A.; Reshchikov, M. A.; Doan, S.; Avrutin, V.; Cho, S. J.; Morkoç, H. *J. Appl. Phys.* **2005**, *98*, 041301.
(2) Kihara, K.; Donnay, G. *Can. Mineral.* **1985**, *23*, 647−654.
(3) Kjekshus, A.; Peterzens, P. G.; Rakke, T.; Andresen, A. F. *Acta Chem. Scand.* **1979**, *A33*, 469−480.
(4) Bates, C. H.; White, W. B.; Roy, R. *Science* **1962**, *137*, 993.
(5) Klingshirn, C. *Phys. Status Solidi B* **2007**, *244*, 3027−3073.
(6) Bunn, C. W. *Proc. Phys. Soc.* **1935**, *47*, 835−842.
(7) Braekken, H.; Jore, C. *The Norwegian Science Scripts* **1935**, *NR8*, 1 (in Norwegian).
(8) Heller, R. B.; McGannon, J.; Weber, A. H. *J. Appl. Phys.* **1950**, *21*, 1283−1284.
(9) Rymer, T. B.; Archard, G. D. *Research* **1952**, *5*, 292.
(10) Cimino, A.; Marezio, M.; Santoro, A. *Die Naturwissenschaften* **1957**, *44*, 348−349.
(11) Gray, T. J. *J. Am. Ceram. Soc.* **1954**, *37*, 534−538.
(12) Mohanty, G. P.; Azároff, L. V. *J. Chem. Phys.* **1961**, *35*, 1268−1270.
(13) Khan, A. A. *Acta Crystallogr., Sect. A: Cryst. Phys., Diffr., Theor. Gen. Crystallogr.* **1968**, *24*, 403−403.
(14) Reeber, R. R. *J. Appl. Phys.* **1970**, *41*, 5063−5066.
(15) Reynolds, D. C.; Collins, T. C. *Phys. Rev.* **1969**, *185*, 1099−1102.
(16) Dietl, T. *Science* **2000**, *287*, 1019−1022.
(17) Pearton, S. J.; Abernathy, C. R.; Thaler, G. T.; Frazier, R. M.; Norton, D. P.; Ren, F.; Park, Y. D.; Zavada, J. M.; Buyanova, I. A.; Chen, W. M.; Hebard, A. F. *J. Phys.:Condens. Matter* **2004**, *16*, 209.
(18) Pearton, S. J.; Heo, W. H.; Ivill, M.; Norton, D. P.; Steiner, T. *Semicond. Sci. Technol.* **2004**, *19*, 59.
(19) Ueda, K.; Tabata, H.; Kawai, T. *App. Phys. Lett.* **2001**, *79*, 988.
(20) Chaboy, J.; Boada, R.; Piquer, C.; Laguna-Marco, M. A.; García-Hernández, M.; Carmona, N.; Llopis, J.; Ruíz-González, M. L.; González-Calbet, J.; Fernández, J. F.; Garca, M. A. *Phys Rev. B* **2010**, *82*, 64411.
(21) Whitaker, K. M.; Raskin, M.; Kiliani, G.; Beha, K.; Ochsenbein, S. T.; Janssen, N.; Fonin, M.; Rüdiger, U.; Leitenstorfer, A.; Gamelin, D. R.; Bratschitsch, R. *Nano Lett.* **2011**, *11*, 3355−3360.
(22) Radovanovic, P.; Gamelin, D. *Phys. Rev. Lett.* **2003**, *91*, 157202.
(23) Kaspar, T.; Heald, S.; Wang, C.; Bryan, J.; Droubay, T.; Shutthanandan, V.; Thevuthasan, S.; McCready, D.; Kellock, A.; Gamelin, D.; Chambers, S. *Phys. Rev. Lett.* **2005**, *95*, 217203.
(24) Weakliem, H. A. *J. Chem. Phys.* **1962**, *36*, 2117−2140.
(25) Koidl, P. *Phys Rev. B* **1977**, *15*, 2493−2499.
(26) Lommens, P.; Smet, P. F.; de Mello Donegá, C.; Meijerink, A.; Piraux, L.; Michotte, S.; Mátéfi-Tempfli, S.; Poelman, D.; Hens, Z. *J. Lumin.* **2006**, *118*, 245−250.

(27) Avramenko, K. A.; Bryksa, V. P.; Strelchuk, V. V.; Deparis, C.; Morhain, C.; Tronc, P. arXiv.org 2011
(28) Schulz, H. J.; Thiede, M. *Phys. Rev. B* **1987**, *35*, 18−34.
(29) McCarthy, P. J.; Güdel, H. U. *Coord. Chem. Rev.* **1988**, *88*, 69−131.
(30) Millot, M.; González, J.; Molina, I.; Salas, B.; Golacki, Z.; Broto, J.; Rakoto, H.; Goiran, M. *J. Alloys Compd.* **2006**, *423*, 224−227.
(31) Tena-Zaera, R.; Martínez-Tomás, M. C.; Hassani, S.; Triboulet, R.; Muñoz-Sanjosé, V. *J. Cryst. Growth* **2004**, *270*, 711−721.
(32) Muñoz-Sanjosé, V.; Tena-Zaera, R.; Martínez-Tomas, C.; Zuñiga-Pérez, J.; Hassani, S.; Triboulet, R. *Phys. Status Solidi C* **2005**, *2*, 1106−1114.
(33) Martínez-Criado, G.; Segura, A.; Sans, J. A.; Homs, A.; Pellicer-Porres, J.; Susini, J. *Appl. Phys. Lett.* **2006**, *89*, 061906.
(34) Yuhas, B. D.; Zitoun, D. O.; Pauzauskie, P. J.; He, R.; Yang, P. *Angew Chem., Int. Ed.* **2006**, *45*, 420−423.
(35) Schwartz, D. A.; Norberg, N. S.; Nguyen, Q. P.; Parker, J. M.; Gamelin, D. R. *J. Am. Chem. Soc.* **2003**, *125*, 13205−13218.
(36) Syassen, K. *High Pressure Res.* **2008**, *28*, 75−126.
(37) Forman, R. A.; Piermarini, G. J.; Barnett, J. D.; Block, S. *Science* **1972**, *176*, 284−285.
(38) Reinen, D. *Struct. Bonding (Berlin)* **1969**, *6*, 30.
(39) Sugano, S.; Tanabe, Y.; Kamimura, H. *Multiplets of transition-metal ions in crystals*; Academic Press: New York, 1970.
(40) Nataf, L.; Rodríguez, F.; Valiente, R. *Phys. Rev. B* **2012**, *86*, 125123.
(41) Ferguson, J. *J. Chem. Phys.* **1969**, *51*, 2904.
(42) Klyucharov, Y. V.; Suvorov, S. A. *Inorg. Mater.* **1965**, *1*, 1281−1286.
(43) Pandey, R.; Gale, J. D.; Sampath, S. K.; Recio, J. M. *J. Am. Ceram. Soc.* **1999**, *82*, 3337−3341.
(44) Bortz, M. L.; French, R. H.; Jones, D. J.; Kasowski, R. V.; Ohuchi, F. S. *Phys. Scr.* **1990**, *41*, 537−541.
(45) Gilliland, S.; Sans, J.; Sánchez-Royo, J.; Almonacid, G.; García-Domene, B.; Segura, A.; Tobias, G.; Canadell, E. *Phys. Rev. B* **2012**, *86*, 155203.
(46) Johnson, C. A.; Kaspar, T. C.; Chambers, S. A.; Salley, G. M.; Gamelin, D. R. *Phys. Rev. B* **2010**, *81*, 125206.
(47) Johnson, C. A.; Cohn, A.; Kaspar, T.; Chambers, S. A.; Salley, G. M.; Gamelin, D. R. *Phys. Rev. B* **2011**, *84*, 125203.
(48) Duan, X. *Opt. Mater.* **2004**, *25*, 65−69.
(49) Yumashev, K. V.; Denisov, I. A.; Posnov, N. N.; Prokoshin, P. V.; Mikhailov, V. P. *Appl. Phys. B: Lasers Opt.* **2000**, *70*, 179−184.
(50) Yumashev, K. V. *Appl. Opt.* **1999**, *38*, 6343−6346.
(51) Serrano, J.; Romero, A.; Manjón, F.; Lauck, R.; Cardona, M.; Rubio, A. *Phys. Rev. B* **2004**, *69* (094306), 1−13.
(52) Rodríguez, F.; Davies, G.; Lightowlers, E. C. *Phys. Rev. B* **2000**, *62*, 6180−6191.
(53) Sans, J. A.; Segura, A.; Sánchez-Royo, J. F.; Ferrer-Roca, C.; Guillotel, E. *Phys. Status Solidi B* **2007**, *244*, 407−412.
(54) Shannon, R. D. *Acta Crystallogr., Sect. A: Cryst. Phys., Diffr., Theor. Gen. Crystallogr.* **1976**, *32*, 751−767.
(55) Han, T. P. J.; Villegas, M.; Peiteado, M.; Caballero, A. C.; Rodríguez, F.; Jaque, F. *Chem. Phys. Lett.* **2010**, *488*, 173−176.
(56) Stefan, M.; Nistor, S. V.; Ghica, D. *Cryst. Growth Des.* **2013**, *13*, 1350−1359.
(57) Park, S. H.; Hanada, T.; Oh, D. C.; Minegishi, T.; Goto, H.; Fujimoto, G.; Park, J. S.; Im, I. H.; Chang, J. H.; Cho, M. W.; Yao, T.; Inaba, K. *Appl. Phys. Lett.* **2007**, *91*, 1904.